
Article:
Kana Padinharu, D.K., Li, G.-J. orcid.org/0000-0002-5956-4033, Zhu, Z.Q. et al. (5 more authors) (2020) Scaling effect on electromagnetic performance of surface mounted permanent magnet Vernier machine. IEEE Transactions on Magnetics. ISSN 0018-9464

https://doi.org/10.1109/TMAG.2020.2980500

Scaling Effect on Electromagnetic Performance of Surface Mounted Permanent Magnet Vernier Machine

D. K. Kana Padinharu[1], G. J. Li[1], *Senior Member, IEEE*, Z. Q. Zhu[1], *Fellow, IEEE*, M. P. Foster[1], D. A. Stone[1], A. Griffo[1], R. Clark[2], and A. Thomas[2]
1, Department of Electronic and Electrical Engineering, The University of Sheffield, Sheffield, UK
2, Siemens Gamesa Renewable Energy Limited, North Campus, Broad Lane, Sheffield, UK
g.li@sheffield.ac.uk.

***Abstract*—This paper investigates the impact of scaling on the electromagnetic performance of Surface Mounted Permanent Magnet Vernier (SPM-V) machines with a main focus on open circuit induced EMF. Three different power ratings, i.e. 3kW, 500kW and 3MW, have been chosen for this study. For each power rating, the SPM-V machines are analyzed for different slot/pole number combinations to compare their optimal performance with a conventional SPM machine. Step by step development of an analytical equation is presented for the prediction of induced EMF taking into account the inter-pole leakage of rotor permanent magnets. 2D Finite Element Analysis (FEA) has been used to validate the analytical equation across different power ratings. The analytical equation is thereafter utilized to study the influence of different geometric parameters on the performance of the SPM-V machines. It reveals that the back EMF and torque of SPM-V machines, for a given normalized pole pitch (rotor pole pitch to magnetic airgap length), is unaffected by the increase in airgap length due to scaling. However, the power factor of SPM-V, unlike the conventional SPM, reduces significantly with increase in electrical loading due to scaling effect. The analytical model for induced EMF and the 2D FEA predicted results are validated by experiments using conventional SPM and SPM-V machine prototypes.**

Keywords—Airgap permeance, analytical modelling, leakage factor, scaling, Vernier machine.

I. Introduction

In recent years, high power direct drive wind generators have become very popular especially for the offshore wind application. This is mainly due to the improved reliability and reduced losses by going gearless [1]–[4]. However, being direct drive, the operating speed of the generator would be very low. This demands the generator size to increase significantly for large power ratings to match the required high torque [2], [5]. Thus, a lot of research is undergoing to reduce the size and weight of the generator by employing solutions, such as superconducting technology [6]–[8] and liquid cooled winding [9], etc.

Another approach proposed in literature is the concept of magnetically geared machines which eliminates a physical gear box and at the same time gives the benefit of high torque density [10], [11]. In [12], this concept has been extended to an outer rotor magnetically geared machine with three airgaps for wind power. Since these machines have more complicated structure due to their double or triple airgap topology, it becomes difficult to implement for high power, e.g. MW level, offshore wind application.

Recently, permanent magnet Vernier machines have gained much attention because of their attractive features such as high torque density and inherently low torque ripple [13]–[15]. Although they work on the same principle as the magnetically geared machines, their structure is much simpler and can be designed with a single airgap. This was made possible by attaching the flux modulating steel pieces (a separate active component in magnetically geared machine) with the stator [16], [17]. A few Vernier machine topologies have been discussed in literature specific to wind power application. A novel 2.2kW, 75rpm direct drive Vernier generator with a split teeth stator and an outer rotor is presented in [17]. Similarly, a 500kW direct drive Vernier generator utilizing a spoke type rotor and open slot stator is discussed in [18], which can achieve a high torque density of 31kNm/m^3. Vernier designs with superconducting technology, targeting at multi-MW wind power generators, have also been discussed in [19], [20].

It is found in literature that most of the research for Vernier machines has been focused on relatively small machines (up to few kW). Moreover, no systematic study has yet been done to understand the performance of Vernier machines with scaling to multi-MW power level in comparison with existing conventional SPM machines. To bridge this research gap, this paper focuses on studying the influence of scaling on SPM-V machine performance compared to the conventional SPM counterpart for a wide range of power ratings, e.g. from 3kW to 3MW. For each power rating, the slot/pole number combination of SPM-V machines is varied in order to achieve the optimal performance.

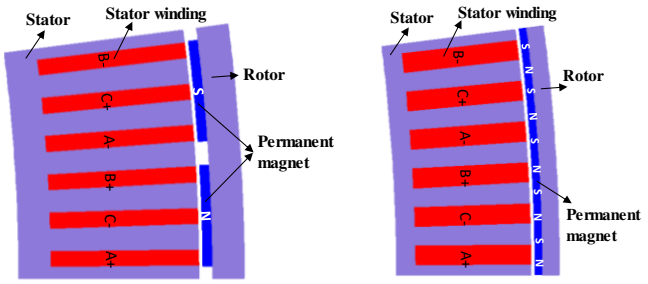

Fig. 1. Comparison of 2D models (one pole pair). (a) conventional SPM machine. (b) SPM-V machine.

II. Machine Topologies and Slot/Pole Number Combinations

For large direct drive wind generator, an outer rotor topology has been proven to be more suitable in terms of structural assembly as the generator rotor can be directly coupled to the turbine blades [21], [22]. This also allows to have multi-pole structure because of its large outer periphery and therefore to achieve better torque density [21]. Because of the above reasons, three direct drive conventional SPM machines having outer rotor topology, as shown in Fig. 1(a), with power ratings of 3kW, 500kW [23] and 3MW [4] are chosen for the scaling study in this paper. A single layer integer slot winding with slots/pole/phase

(SPP) equal to 1 has been adopted for all the power ratings. The key parameters of the machines are given in TABLE I.

The airgap length is critical for the scaling study and it is maintained as 0.1% of the airgap diameter which is the widely accepted thumb rule [24]. Also, to avoid any effect of aspect ratio (machine active length over airgap diameter) on the scaling study, their value is maintained the same for the investigated power ratings. Although the 3MW design in [4] is with an inner rotor, to be consistent with other power ratings, it has been converted to an outer rotor topology. For each power rating, the SPM-V machines, as shown in Fig. 1(b), are designed to have the same rotor outer diameter, phase current, copper loss and magnet volume as the conventional SPM.

TABLE I. KEY PARAMETERS OF SPM MACHINE

	3kW	500kW	3MW
Rated speed(rpm)	170	32	15
Rotor outer diameter(mm)	426.4	2195.5	5000
Airgap length (mm)	0.5	2.15	5
Stack length(mm)	100	550	1200
Aspect ratio		0.25	
Magnet volume(m^3)	0.000408	0.0162	0.227
Phase current(Arms)	2.7	438	2694
Electrical loading(AT/mm)	9.3	62.7	58.6
Turns/phase	720	161	56

For the conventional integer slot SPM machine, the rotor pole pair number (P_r) is the same as the stator winding pole pair number (P_s) to achieve synchronous speed and to produce electromagnetic torque. However, in a SPM-V machine the slot/pole number combinations follow the rule described by [13], [25]:

$$P_r = Z - P_s \text{ or } P_r = Z + P_s \tag{1}$$

where Z is the number of stator slots. This enables the Vernier machine to utilize the magnetic gearing effect also called modulation effect to produce high torque. For demonstration, the magnetic gearing effect of the SPM-V machine for the specific case where $P_r = (Z - P_s)$ with $Z = 6, P_r = 5$ and $P_s = 1$ is shown in Fig. 2(b). The structure of the SPM-V machine with this slot/pole number combination is shown in Fig. 2(a).

The low speed direct drive rotor with $P_r = 5$ is rotating at a mechanical speed of ω_r. The 5 pole pair airgap field created by the permanent magnets is then modulated by the $Z = 6$ (open slot) stator teeth (airgap permeance). The resultant modulated flux will have, in addition to the fundamental (P_r^{th} order) harmonic, a subharmonic airgap field component of $(Z - P_r)^{\text{th}}$ order. This one pole pair modulated magnetic flux distribution is shown in Fig. 2(a). This field will rotate at an angular speed of $[P_r/(Z - P_r)]\omega_r$ (in this case $5\omega_r$), creating a virtual high speed rotor. This mimics the action of a gearbox and therefore a small physical movement of the rotor results in fast changing modulated field. This fast changing flux is utilized by Vernier machines to generate high torque. For steady torque production, the stators are wound such that they match the modulated airgap field pole pair number ($Z - P_r = P_s = 1$) and are excited with a frequency equal to $P_r\omega_r$. This will make the armature field rotate at the same mechanical speed as the modulated field generated by permanent magnets. The ratio of the speed of the high speed virtual rotor over that of the low speed direct drive rotor is defined as the gear ratio (G_r) of a Vernier machine (in this case $G_r = 5$) and is given by

$$P_r = Z - P_s \text{ or } P_r = Z + P_s \tag{2}$$

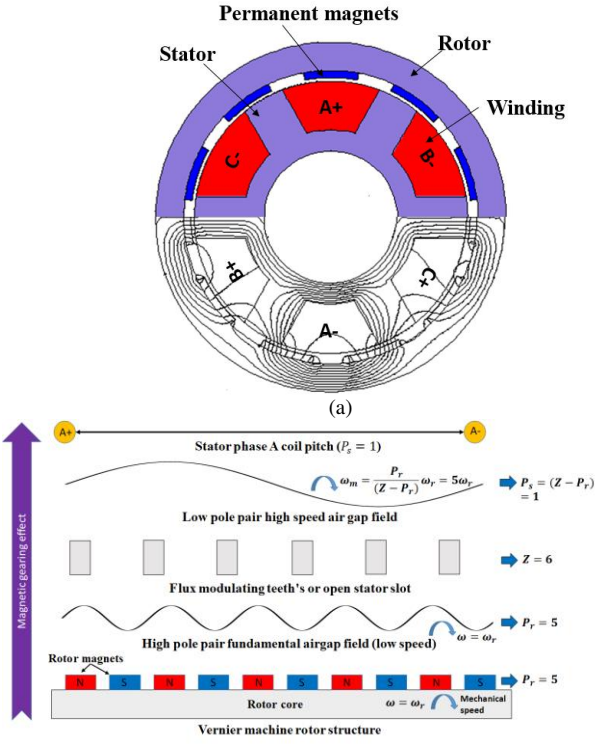

Fig. 2. (a) SPM-V machine with slot/pole number $Z = 6, P_r = 5$ and $P_s = 1$ with the open circuit flux distribution highlighted. (b) Schematic showing the magnetic gearing effect in SPM-V machine with slot/pole number following the rule, $P_r = Z - P_s$.

It has been proven that the Vernier machine designed with slot/pole number combination given by $P_r = Z - P_s$ generates higher torque compared to the one with $P_r = Z + P_s$ [13]. Therefore, to maximize the torque density, the slot/pole number combinations selected for this study will be $P_r = (Z - P_s)$. Moreover, a gear ratio of 5 has been selected as this is a popular gear ratio widely used in literature [25]–[30].

Different slot/pole number combinations used for Vernier machines, which satisfy the aforementioned rule, are given in TABLE II. All the designs, including the conventional SPM, are globally optimized using OPERA Optimizer tool for maximum torque production. This optimization tool uses a combination of deterministic (sequential quadratic programming) and stochastic methods (genetic algorithms, simulated annealing). The definitions of the variables used for the global optimization are as follows: λ_s is the split ratio, M_{th_ratio} is the magnet thickness ratio, M_{arc_ratio} is the magnet pole arc ratio, $S_{op_ratio}$is the slot open ratio and S_{bk_ratio} is the stator back iron thickness ratio.

$$\lambda_s = \frac{D_{ri}}{D_{ro}} \tag{3}$$

$$M_{th\_ratio} = \frac{h_m}{h_m + h_{yr}} \tag{4}$$

$$M_{arc\_ratio} = \frac{w_m}{\tau_r} \tag{5}$$

TABLE II. SLOT/POLE NUMBER COMBINATIONS

Machine Type	Design number	3kW			500kW			3MW		
		N_s	P_r	P_s	N_s	P_r	P_s	N_s	P_r	P_s
Conventional	0	96	16	16	294	49	49	480	80	80
Vernier	1	12	10	2	42	35	7	48	40	8
Vernier	2	24	20	4	84	70	14	60	50	10
Vernier	3	36	30	6	126	105	21	72	60	12
Vernier	4	48	40	8	168	140	28	96	80	16
Vernier	5	72	60	12	210	175	35	120	100	20
Vernier	6	96	80	16	252	210	42	192	160	32
Vernier	7	120	100	20	294	245	49	240	200	40
Vernier	8							360	300	60
Vernier	9							480	400	80

$$S_{op\_ratio} = \frac{b_o}{\tau_s} \tag{6}$$

$$S_{bk\_ratio} = \frac{h_{ys}}{h_{ys} + h_t} \tag{7}$$

where D_{ri} is the rotor inner diameter, $D_{ro}$is the rotor outer diameter. Other variables used in (4) to (7) are illustrated in Fig. 3. Rotor outer diameter (D_{ro}) and airgap length (g) are fixed across slot/pole number combinations for a given power rating.

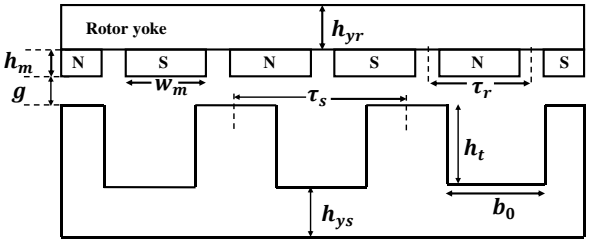

Fig. 3. Schematic of geometric parameters.

The methodology adopted for this study is as per the steps given below

(a) Develop analytical equation for induced EMF
(b) Validate with 2D FEA for all power ratings across different slot/pole number designs of SPM-V
(c) Use final analytical equation for studying the influence of scaling
(d) Verify the conclusion with 2D FEA

It is worth noting that the objective of developing an analytical equation is to get more insight into the geometric parameters influencing the performance of SPM-V machine due to scaling effect. In the analytical modelling, the introduction of a new permeance function and leakage factor for the calculation of induced EMF adds extra novelty to this paper.

III. Baseline Analytical Equation

A. Permeance Function Validation

Vernier machine, as explained in section II, works on the principle of flux modulation to generate the induced EMF [16]. For a machine designed with a slot/pole number combination governed by $Z - P_r = P_s$, the working airgap flux density harmonics contain two main components [31], i.e. (a) modulated PM flux densities (B_{Z-P_r} and B_{Z+P_r}) of $(Z - P_r)^{\text{th}}$ and $(Z + P_r)^{\text{th}}$ orders and (b) fundamental PM flux density (B_{P_r}) of the order $(P_r)^{\text{th}}$. As an example, the typical radial airgap flux density spectrum of a Vernier machine for one pole-pair model (for example, $Z = 6, P_r = 5, P_s = 1$) with the working harmonics highlighted is shown in Fig. 4. Neglecting the contribution from $(Z + P_r)$ term, as done in most literature, the RMS (root mean square) value of induced EMF per phase (E_{ph-v}) for an SPM-V machine can be written as [25], [32]

$$E_{ph-v} = \frac{k_w T_{ph} \omega_m D_g L_{stk}}{\sqrt{2}} \left(G_r B_{Z-P_r} + B_{P_r}\right) \tag{8}$$

where k_w is the fundamental winding factor, T_{ph} is the number of series turns per phase, ω_m is the rotor mechanical angular velocity, D_g and L_{stk} are the airgap diameter and stack length, respectively. The winding factor (k_w) for this study is equal to 1 as the single-layer integer-slot winding is used in all the designs.

The airgap flux density harmonics can be expressed in terms of airgap permeance and fundamental PM MMF (F_1) as [13]

$$\begin{cases} B_{P_r} = F_1 \Lambda_0 \\ B_{Z-P_r} = \dfrac{1}{2} F_1 \Lambda_1 \end{cases} \tag{9}$$

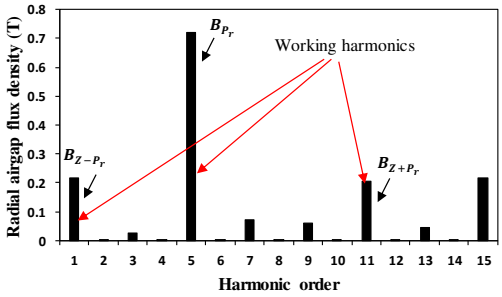

Fig. 4. Typical radial airgap flux density of Vernier machine with one pole-pair model having $Z = 6, P_r = 5, P_s = 1$.

where Λ_0 is the DC component and Λ_1 is the peak fundamental of the airgap permeance. Combining (8) and (9) gives

$$E_{ph-v} = \frac{k_w T_{ph} \omega_m D_g L_{stk} (F_1 \Lambda_0)}{\sqrt{2}} \left(\frac{G_r}{2} \Lambda_r + 1\right) \tag{10}$$

where Λ_r is defined as the ratio of Λ_1 to Λ_0.

The first term in the brackets of (10) represents the extra EMF component produced in the Vernier machine compared to the conventional machine. The calculation of induced EMF in (10) largely depends on the accuracy of the airgap permeance function. Most of the existing analytical modeling for Vernier machine has used the permeance function as given in [33], which is originally derived for induction machine with small airgap. Although this permeance function produces accurate result for Vernier machines [29], [31] with relatively small airgap, may not be suitable for higher power ratings with larger airgap length. This permeance function was later modified in [34] by considering the variation of permeance along the radial direction of airgap to suit the permanent magnet machines.

Similarly, a permeance function was derived for Vernier machine in [35] from [33] by replacing the linear airgap model to a more realistic cylindrical airgap considering radial variation of magnetic field. However in all the above analytical models, the permeance function distribution is assumed to be sinusoidal within the slot opening. Moreover, the effect of slot opening on magnetic field distribution is assumed to be extended till $0.8b_0$ (a fixed value derived from induction machine) from the center of the slot. These assumptions may not be accurate while considering a wide range of slot/pole number combinations for Vernier machines.

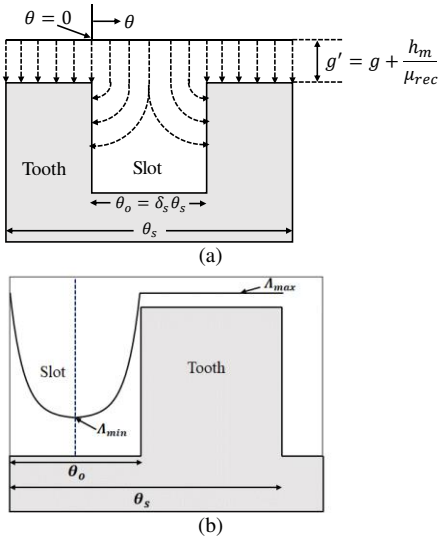

Fig. 5. (a) Flux lines for calculating the airgap permeance. (b) Schematic of new airgap permeance function having an exponential variation of permeance between the maximum (Λ_{max}) value facing stator tooth and the minimum value (Λ_{min}) facing stator slot.

Different from the above approaches, a permeance function is presented in [36] assuming a quarter circular contour for flux lines underneath the stator slot [as shown in Fig. 5(a)]. The permeance function $[\Lambda(\theta)]$, is given by

$$\Lambda(\theta) = \mu_o / \left[g' + l_g(\theta)\right] \tag{11}$$

With

$$l_g(\theta) = \begin{cases} \dfrac{\pi R_{si}}{2} \dfrac{\sin(\theta/2)\sin(\delta_s\theta_s/2 - \theta/2)}{\sin(\delta_s\theta_s/4)\cos(\theta/2 - \delta_s\theta_s/4)}, & \theta \in [0, \delta_s\theta_s] \\ 0, & \theta \in [\delta_s\theta_s, \theta_s] \end{cases} \tag{12}$$

where $g' = g + h_m/\mu_{rec}$ is the magnetic airgap length with g being the mechanical clearance, h_m and μ_{rec} are the magnet thickness and recoil permeability, respectively; $l_g(\theta)$ is the extra effective airgap length underneath the stator slot which the flux lines need to traverse beyond the magnetic airgap length g', R_{si} is the stator outer radius, θ is the mechanical angle, δ_s is the slot pitch ratio defined as the ratio of slot opening (b_o) to slot pitch (τ_s), θ_s is slot pitch angle. This permeance function has been proven to be accurate for machines with small airgap length [37]. However, it does not give simple expressions for permeance coefficients using Fourier series analysis which are critical for understanding the influence of geometric parameters. Hence, a new permeance function is proposed in this paper which assumes an exponential variation between Λ_{max} (maximum value of the permeance function) and Λ_{min} (minimum value of the permeance function) derived from [36], as shown in Fig. 5. As Vernier machines are generally designed with large number of rotor poles (see TABLE II), the chance of getting saturated under open circuit condition is very small. Hence the effect of saturation on permeance calculation has been neglected for this study. The proposed permeance function is given by

$$\Lambda(\theta) = \begin{cases} \Lambda_d e^{-2u\theta/\theta_o} + \Lambda_{min} & ,\theta \in [0, \theta_o/2] \\ \Lambda_d e^{-2u(\theta_o-\theta)/\theta_o} + \Lambda_{min} & ,\theta \in [\theta_o/2, \theta_o] \\ \Lambda_{max} & ,\theta \in [\theta_o, \theta_s] \end{cases} \tag{13}$$

with

$$\Lambda_d = \Lambda_{max} - \Lambda_{min} \tag{14}$$

and

$$\Lambda_{max} = \frac{\mu_o}{g'} \tag{15}$$

$$\Lambda_{min} = \frac{\mu_0}{g' + \dfrac{\pi R_{si}}{2}\sin\left(\dfrac{\theta_o}{4}\right)} \tag{16}$$

where $\theta_o = \delta_s\theta_s$ is the stator slot opening angle. The exponential variation is a function of the geometric parameters represented by the variable u as

$$u = 6 \Big/ \left(1 + \frac{g'}{b_o}\right) \tag{17}$$

The Fourier series analysis coefficients for the proposed permeance function can be easily derived and thereby simple expressions for Λ_0 and Λ_1 can be achieved as described by

$$\Lambda_0 = \Lambda_{max} + \Lambda_d\delta_s\left(\frac{1 - e^{-u}}{u} - 1\right) \tag{18}$$

and

$$\Lambda_1 = \frac{C_o^2}{C_o^2 + \delta_s^2}\frac{2\Lambda_d\delta_s}{u}\left(\frac{\pi\delta_s}{u} - e^{-u}\right) - \frac{2\Lambda_d}{\pi} \text{ with } C_o = \frac{u}{\pi} \tag{19}$$

This proposed permeance function as described by (13) is then validated by FEA and also with the Method 2 [35] and Method 3 [36]. It is worth noting that the permeance function calculated by FEA is under linear condition by adopting the methodology described in [37]. The comparison of the four methods has been done by evaluating the permeance function for the 500kW Vernier machine with three different slot/pole number combinations, as shown in Fig. 6. These three slot/pole number combinations would cover a wide range of slot opening (b_o) to airgap length (g) ratios. It can be observed from Fig. 6 that the permeances predicted by the new proposed method and by Method 3 are in good agreement with the FEA predictions. However, a sinusoidal approximation of permeance function by Method 2 is showing significant deviation from the FEA results. Moreover, the minimum value of permeance function at the centre of stator slot predicted by Method 2 is significantly different from FEA towards higher slot/pole number.

The comparison of the calculated permeance coefficient Λ_0 and the permeance ratio $\Lambda_r = \Lambda_1/\Lambda_0$, for the 500kW Vernier machine for all slot/pole number combinations are shown in Fig. 7. The comparison shows that the proposed method is in good agreement with the FEA for the calculation of Λ_0. However, there is minor discrepancy observed in the calculation of Λ_r, particularly towards high

slot/pole number designs. This is largely due to the higher fringing effect observed over a wider span of the stator tooth area for larger slot/pole numbers, as shown in Fig. 6.

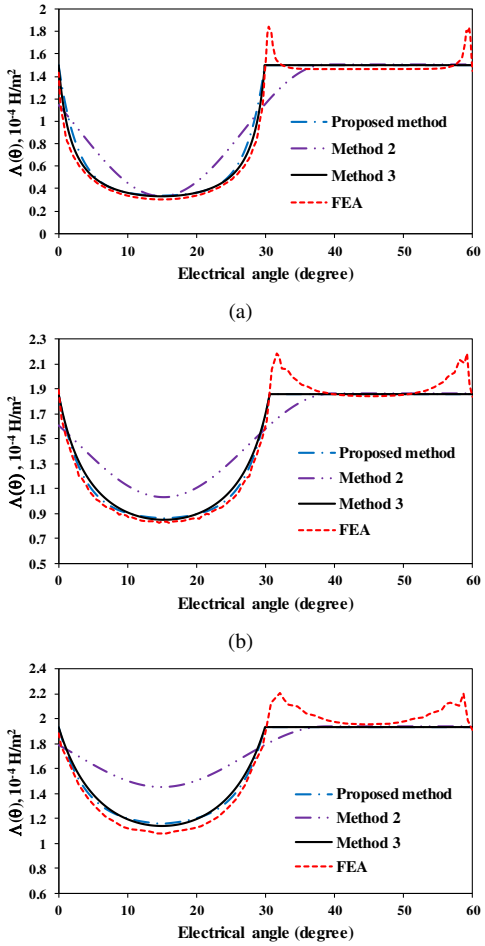

Fig. 6. Comparison of proposed permeance function with FEA, Method 2 [35] and Method 3 [36] using the 500kW Vernier machine with slot/pole number (a) $N_s = 42, P_r = 35, P_s = 7$. (b) $N_s = 168, P_r = 140, P_s = 28$. (c) $N_s = 294, P_r = 245, P_s = 49$.

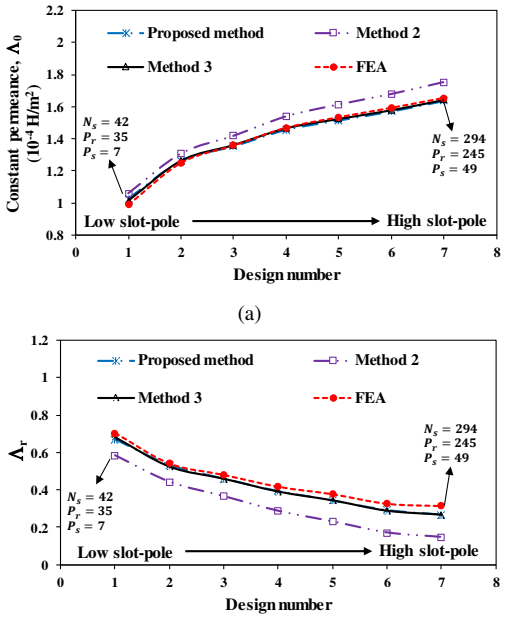

Fig. 7. Comparison of permeance coefficients (a) Λ_0 (b) Λ_r calculated by the newly proposed method, FEA, Method 2 [35] and Method 3 [36] for the 500kW Vernier machine with different slot/pole numbers. The x-axis is the design number as quoted in TABLE II.

Nonetheless, the predictions are very much matching with that of the Method 3 [36], which cannot provide simple analytical expressions for the permeance coefficients [as in (18) and (19)] required for scaling study.

B. Validation of Induced EMF Calculation

The fundamental magnet MMF (F_1) in (10) can be calculated as [34], [38]

$$F_1 = \frac{4}{\pi}\frac{B_r h_m}{\mu_o \mu_{rec}} \sin\left(\frac{\pi \alpha_p}{2}\right) \tag{20}$$

where B_r is the remanence, α_p is the magnet arc coefficient, i.e. magnet arc to rotor pole pitch (τ_r) ratio.

The proposed permeance function is then used to calculate the induced EMF as described by (10) for all the three selected power ratings. The comparison of the analytically calculated EMF (peak value) with that predicted by FEA is shown in Fig. 8. It is obvious that although the permeance coefficients match well, the analytically calculated EMF is significantly different from the FEA predictions. Moving from 3kW to 3MW, the maximum deviation changes from 26% to 93%.

The next section addresses the reasons for this deviation and a final induced EMF equation will be presented. Step by step improved analytical calculations will be compared with the baseline result achieved in this section and FEA to show the influence of each step on induced EMF prediction.

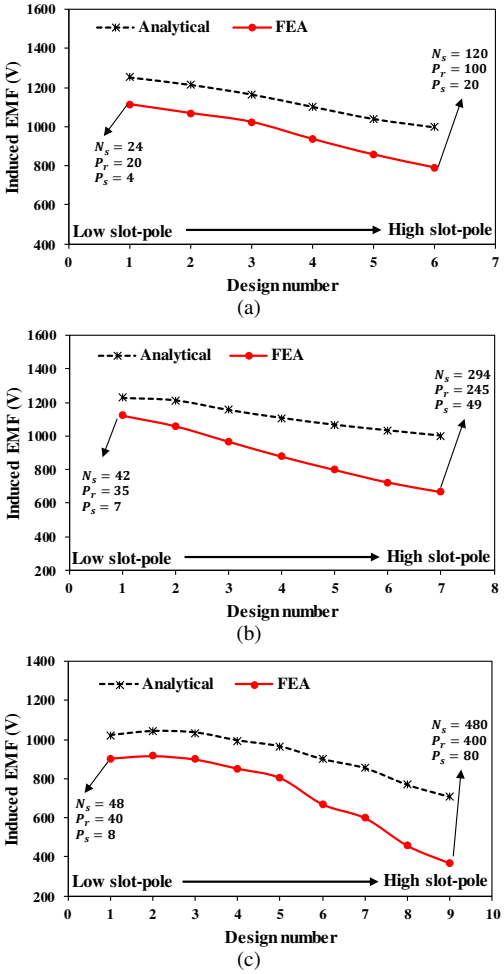

Fig. 8. Comparison of analytical and FEA methods for the calculation of induced EMF for Vernier machine with power ratings (a) 3kW, (b) 500kW and (c) 3MW. The x-axis is the design number as quoted in TABLE II.

IV. Improvement of Analytical Calculation

A. Influence of $(Z + P_r)^{th}$ Working Harmonic

The $(Z + P_r)^{th}$ working harmonic was neglected in section III for the induced EMF calculation. The waveforms of radial airgap flux density working harmonics from FEA for the highest and lowest slot/pole number designs of the 500kW Vernier machine are shown in Fig. 9(a) and (b), respectively. The flux density waveforms are shown for one coil pitch of the phase A. The spectrum comparison of these waveforms is shown in Fig. 9(c). It is observed that, although the fundamental (P_r^{th}) harmonics are comparable between the two machines, the $(Z + P_r)$ term becomes significantly higher for lower slot/pole design. Therefore, this working harmonic cannot be neglected anymore. The induced EMF after considering the $(Z + P_r)$ term can be given as [25]

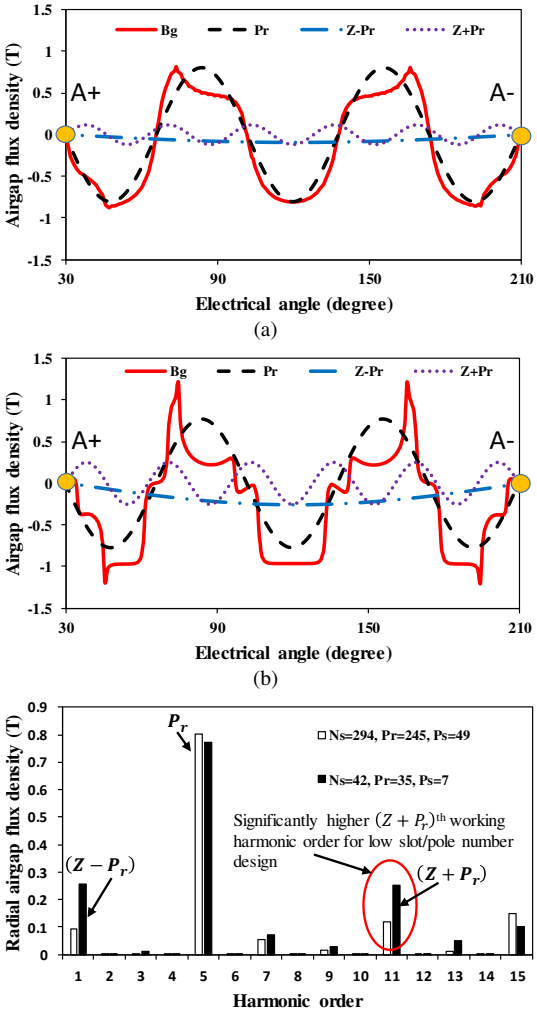

Fig. 9. Comparison of working radial airgap flux density harmonic waveforms of 500kW Vernier machines with slot/pole number (a) $N_s = 294, P_r = 245, P_s = 49$ and (b) $N_s = 42, P_r = 35, P_s = 7$. The comparison of their spectra is shown in (c).

$$E_{ph-v} = \frac{k_w T_{ph} \omega_m D_g L_{stk}}{\sqrt{2}} \left(G_r B_{Z-P_r} + B_{P_r} - \frac{P_r}{(P_r + Z)} B_{Z+P_r} \right) \quad (21)$$

For an integer-slot Vernier machine, the rotor pole-pair number (P_r) and stator slot number (Z) can be expressed in terms of gear ratio (G_r) and stator winding pole-pair (P_s) as

$$P_r = G_r P_s \text{ and } Z = P_r + P_s = (G_r + 1) P_s \quad (22)$$

Substituting (22) in (21), the induced EMF becomes

$$E_{ph-v} = \frac{k_w T_{ph} \omega_m D_g L_{stk}}{\sqrt{2}} \left(G_r B_{Z-P_r} + B_{P_r} - \frac{G_r}{(2G_r + 1)} B_{Z+P_r} \right) \quad (23)$$

Moreover, the magnitudes of modulated flux densities B_{Z-P_r} and B_{Z+P_r} are the same and are equal to $\frac{1}{2} F_1 \Lambda_1$ [31], which simplifies (23) as

$$E_{ph-v} = \frac{k_w T_{ph} \omega_m D_g L_{stk} B_{P_r}}{\sqrt{2}} \left(\frac{G_r^2}{(2G_r + 1)} \Lambda_r + 1 \right) \quad (24)$$

B. Influence of Leakage Factor for Vernier Machine

The analytical equation derived in section III neglects any inter-pole leakage flux of the magnets. A comparison of the open circuit flux distribution between a conventional SPM and SPM-V machines $(N_s = 294, P_r = 245, P_s = 49)$ for 500kW power rating is shown in Fig. 10. The inter-pole leakage in a Vernier machine especially with high slot/pole number is significantly higher than that of a conventional SPM machine. Hence the consideration of a leakage factor is very critical for accurate EMF calculation.

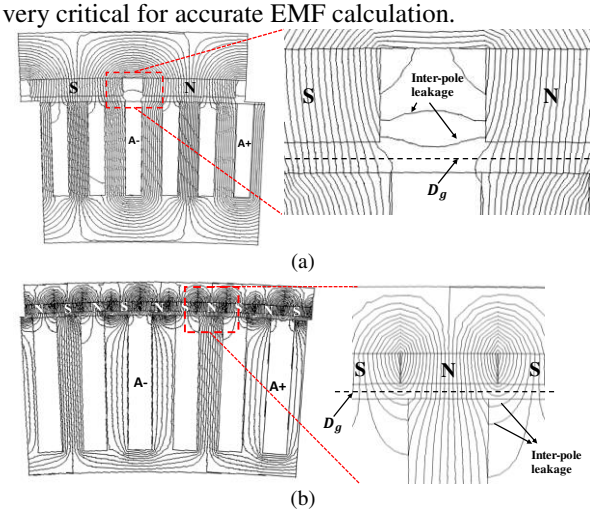

Fig. 10. Comparison of flux distributions under open-circuit condition for 500kW power between (a) conventional SPM machine and (b) Vernier machine with slot/pole number.

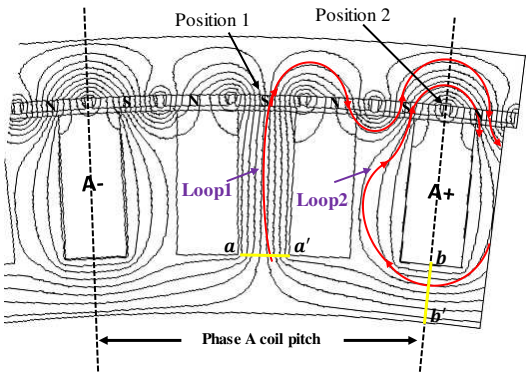

Fig. 11. Open-circuit flux distribution for a Vernier machine showing two major flux loops (loop1 and loop2) contributing to the induced EMF. Flux is extracted from contours aa' and bb' (highlighted in yellow solid line) to show that loop1 and loop2 have the same flux magnitude. Leakage factor is derived from position 1 where magnet is aligned with the stator tooth.

A simple analytical equation is developed for the leakage factor considering the open circuit flux distribution. Unlike the conventional SPM, Vernier machine with $G_r = 5$ has 5 magnet poles under one coil pitch. Since the relative position of each magnet to the stator tooth are different, it is critical to find the right position of the magnets with respect to stator tooth to develop the leakage factor. The open-circuit flux distribution for one coil pitch with phase A having the maximum flux linkage is shown in Fig. 11.

A closer look at the flux distribution reveals that there are two main flux loops, loop1 and loop2 (marked in red arrowed contours), which contributes to the induced EMF of the phase A. Also the flux loops are symmetrical with respect to the middle magnet which is aligned with the stator tooth (position 1 in Fig. 11). The loop1 flux is generated where the magnet is aligned with stator tooth (position 1) and loop2 flux is generated where the inter-pole magnet axis is aligned with the middle of stator slot (position 2 in Fig. 11). To compare their magnitudes, flux lines are extracted from contour aa' and bb' as shown in Fig. 11 for all the slot/pole number combinations of the 500kW Vernier machine. The contour aa' represents the flux which is twice of the loop1 flux and bb' represents the flux which is the sum of loop1 and loop2 fluxes. The comparison of flux extracted from contour aa' and bb' is shown in Fig. 12, which confirms that loop1 and loop2 fluxes have the same magnitude. This exercise reveals that the total flux linking the phase A and generating the induced EMF can be derived by knowing either loop1 flux or loop2 flux. This also means that the calculation of the leakage factor can be done either from position 1 or position 2. For this study, position 1 has been selected as it is symmetrical from the center of the magnet and makes it simple to derive the leakage factor.

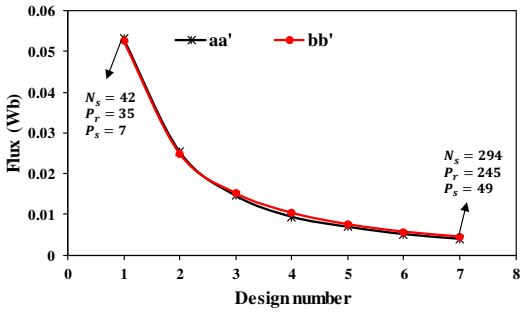

Fig. 12. Comparison of flux values extracted from contours aa' and bb' (see Fig. 11) for 500kW Vernier machine for different slot/pole number combinations. The x-axis is the design number as quoted in TABLE II.

Focusing on the flux lines at position 1 (Fig. 11), the leakage factor can be derived as shown in Fig. 14. Here the section of magnet that generates leakage flux is assumed to span over a distance of $2g$ over one magnet pole pitch. The leakage factor (K_{fl}) is given by

$$K_{fl} = \frac{\tau_r - 2g}{\tau_r} \tag{25}$$

In general, Vernier machines have rotor pole pair number very close to stator slot number. Moreover, the optimal slot pitch ratio for the SPM-V largely falls in the range from 0.4 to 0.6 as shown in Fig. 13. This makes the stator tooth width almost the same as the rotor pole pitch. Although the leakage flux also depends on the stator tooth width, because of the above practical consideration and to simplify the analytical modelling of the leakage factor, any variation in stator tooth width is not considered in the leakage factor.

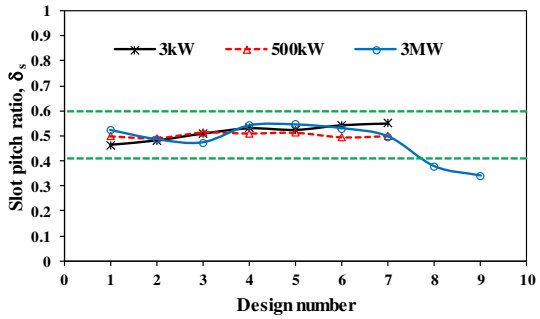

Fig. 13. Comparison of optimal slot pitch ratio (δ_s) for different power ratings across slot/pole number combinations.

After the inclusion of leakage factor, the final induced EMF equation is given by

$$E_{ph-v} = \frac{k_w T_{ph} \omega_m D_g L_{stk} B_{P_r} K_{fl}}{\sqrt{2}} \left(\frac{G_r^2}{(2G_r + 1)} \Lambda_r + 1 \right) \tag{26}$$

The incremental improvements derived from step1 and step2 are individually plotted along with the baseline calculation (from section III) to compare with the FEA, as shown in Fig. 15. The comparison shows that the consideration of the above two factors, i.e. $(Z + P_r)^{\text{th}}$ working harmonic and leakage factor K_{fl}, completely bridges the deviation shown for the baseline analytical calculation in section III. As aforementioned, the impact of $(Z + P_r)^{\text{th}}$ working harmonics is more pronounced for the low slot/pole number designs whereas the leakage factor is largely impacting the high slot/pole number designs.

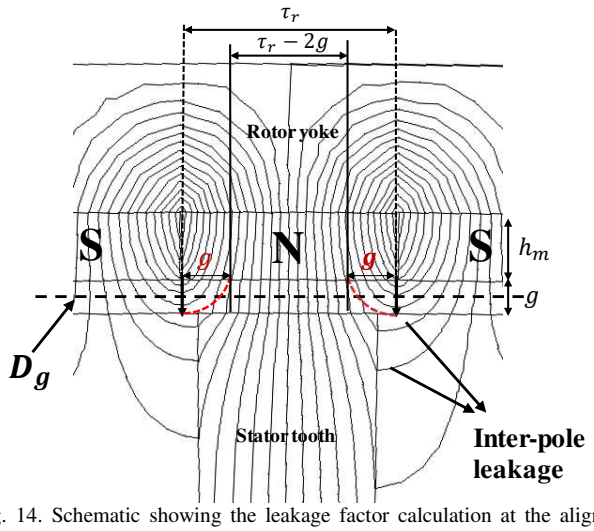

Fig. 14. Schematic showing the leakage factor calculation at the aligned position of magnet with stator tooth. The section of the magnet that generates leakage flux is assumed to span over a distance of $2g$ over one magnet pole pitch (marked by red dotted line).

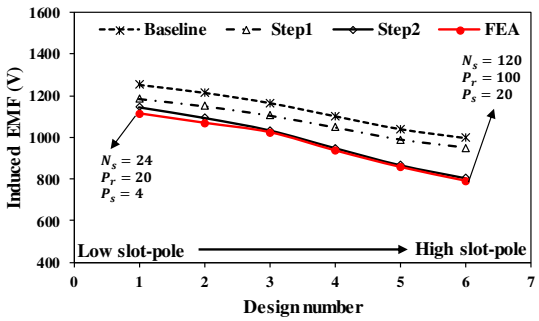

(a)

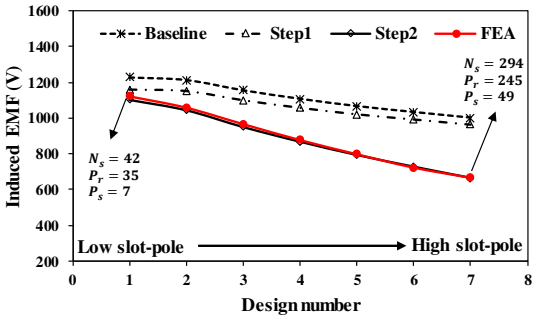

(b)

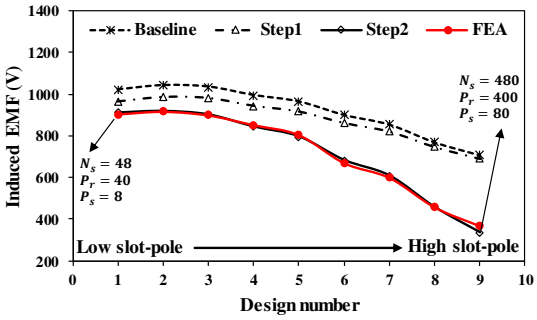

(c)

Fig. 15. Comparison of analytical equation with FEA, showing incremental improvement after taking step1 [consideration of $(Z + P_r)$ harmonic] and step2 (consideration of leakage factor,K_{fl}), for power ratings (a) 3kW (b) 500kW and (c) 3MW Vernier machines. The x-axis is the design number as quoted in TABLE II.

V. Scaling Study for Vernier Machine

A. Phase EMF

For the scaling study, the induced EMFs (E_{ph-v}) of Vernier machines are represented using per unit (PU) values with their respective conventional machines' EMF (E_{ph-c}) being the reference. For an ideal case, assuming the same airgap flux density (B_{P_r}) and airgap diameter (D_g) between SPM-V and conventional SPM machines, the PU induced EMF (E_{ph-PU}) is given by

$$E_{ph-PU} = \frac{E_{ph-v}}{E_{ph-c}} = K_{fl}\left(\frac{G_r^2}{(2G_r+1)}\Lambda_r + 1\right) \tag{27}$$

For a given gear ratio, the performance of Vernier machine across different power ratings largely depends on the K_{fl} and Λ_r values. Substituting (14), (15) and (16) in (18) and (19) and applying

$$R_{si}\sin\left(\frac{\theta_o}{4}\right) = \frac{b_o}{4\cos\frac{\theta_o}{4}} \tag{28}$$

Λ_r becomes

$$\Lambda_r = \frac{2}{\pi}\frac{(1-K)\left[\frac{\delta_s^2}{C_o^2+\delta_s^2}\left(1 - C_o\frac{e^{-u}}{\delta_s}\right) - 1\right]}{(1-K)\delta_s\left(\frac{1-e^{-u}}{u} - 1\right) + 1} \tag{29}$$

where $K$is given by

$$K = \frac{1}{1 + \frac{\pi}{8}\left(\frac{b_o}{g'}\right)\frac{1}{\cos\left(\frac{\theta_o}{4}\right)}} \tag{30}$$

The slot opening ratio (δ_s) is almost constant across power ratings as shown in Fig. 13. As the value of slot opening angle (θ_o) is negligible compared to 2π, the magnitude of $\cos\left(\frac{\theta_o}{4}\right)$ in (30) is almost equal to 1 as shown in Fig. 16 and can be considered as constant across power ratings.

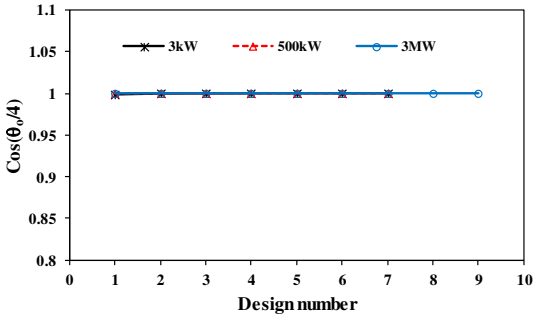

Fig. 16. Comparison of value of $\cos(\theta_0/4)$ across slot/pole number for different power ratings.

From (29), assuming that the slot opening ratio (δ_s) and $\cos\left(\frac{\theta_o}{4}\right)$ is maintained the same across power ratings, it can be concluded that Λ_r is a function of the slot opening (b_o) to the magnetic airgap length (g') ratio. This ratio for a Vernier machine can also be represented as (see Appendix)

$$\frac{b_o}{g'} = \frac{2G_r}{G_r+1}\delta_s\bar{\tau_r} \tag{31}$$

where $\bar{\tau_r}$ is defined as the normalized pole pitch given as

$$\bar{\tau_r} = \frac{\tau_r}{g'} \tag{32}$$

Therefore for different power ratings, the term Λ_r can be regarded as constant for a given normalized pole pitch, as shown in Fig. 17. The representation of slot/pole numbers of SPM-V machines in terms normalized pole pitch will make the scaling study very generic and can give more insight into the design of SPM-V machine for which the performance is poorly understood for high power ratings.

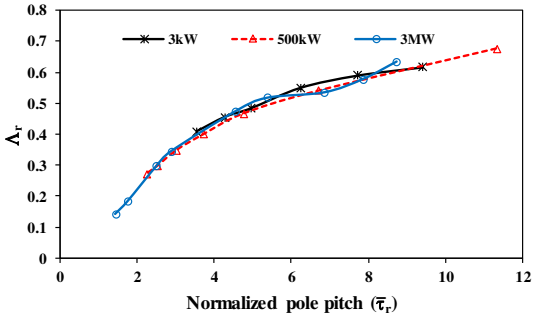

Fig. 17. Variation of Λ_r against normalized pole pitch for different power ratings.

The normalized pole pitch should also largely define the amount of inter-pole magnet leakage. However, for the same normalized pole pitch as conventional SPM machine, the SPM-V machine will have 5 magnets (for gear ratio 5) under one coil pitch. This makes the variation of leakage flux quite complex unlike conventional machine and is not straight forward. Thus the variation of leakage factor (K_{fl}) with normalized pole pitch was further investigated.

The leakage factor (K_{fl}) in (27) is a function of the rotor pole pitch (τ_r) and the airgap length (g) as given in (25). The leakage factor can also be represented in terms of normalized pole pitch as

$$K_{fl} = \frac{\bar{\tau_r} - 2\frac{g}{g'}}{\bar{\tau_r}} \tag{33}$$

The term $2g/g'$ is not a constant for a given normalized pole pitch as shown in Fig. 18(a). However, at high normalized pole pitch, the value of $2g/g'$ is negligible compared to $\bar{\tau_r}$ making the numerator $(\bar{\tau_r} - 2g/g')$ almost the same across power ratings for a given $\bar{\tau_r}$. This brings the leakage factor to near unity for high normalized pole pitch due to negligible leakage compared to flux per pole. Towards lower normalized pole pitch, the $2g/g'$ values are almost similar between different power ratings making the $(\bar{\tau_r} - 2g/g')$ factor nearly constant for a given $\bar{\tau_r}$. The variation of the numerator $(\bar{\tau_r} - 2g/g')$ with $\bar{\tau_r}$ is shown in Fig. 18(b). It can be observed that $(\bar{\tau_r} - 2g/g')$ is almost constant across power ratings for a given $\bar{\tau_r}$. Therefore the leakage factor is almost constant for a given $\bar{\tau_r}$ across power ratings as shown in Fig. 18(c). From the physics point of view, the normalized pole pitch largely defines the amount of inter pole leakage per pole of the machine. As both K_{fl} and Λ_r are almost constant across power ratings for a given $\bar{\tau_r}$, the E_{ph-PU} in (27) should remain the same across different power ratings for a given $\bar{\tau_r}$.

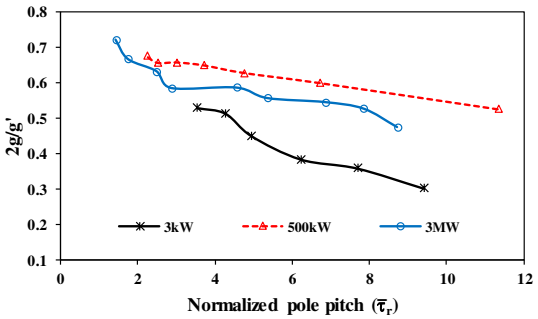

(a)

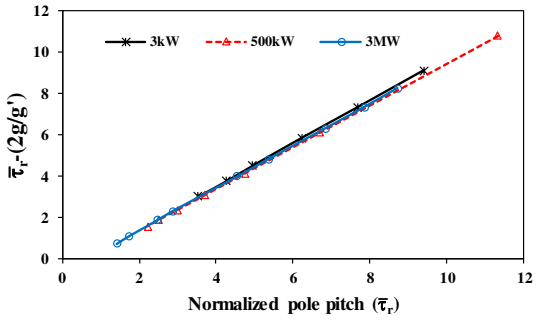

(b)

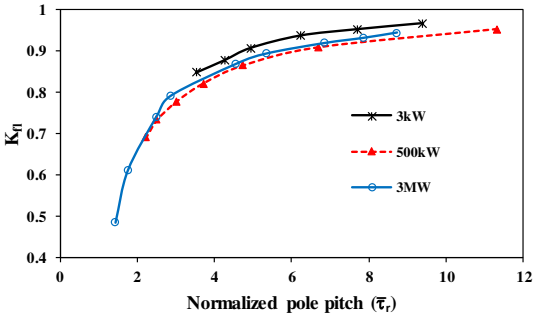

(c)

Fig. 18. Variation of (a) $2g/g'$, (b) $\bar{\tau_r} - (2g/g')$ and (c) K_{fl} against normalized pole pitch for different power ratings.

To verify the above conclusion, the E_{ph-PU} calculated using (27) are compared between different power ratings with their slot/pole numbers represented using normalized pole pitch and are shown in Fig. 19(a). The comparison shows that although there is a significant change in the airgap length from 3kW (0.5mm) to 3MW (5mm), the induced EMF performance with respect to their conventional counterpart is almost the same for a given normalized pole pitch.

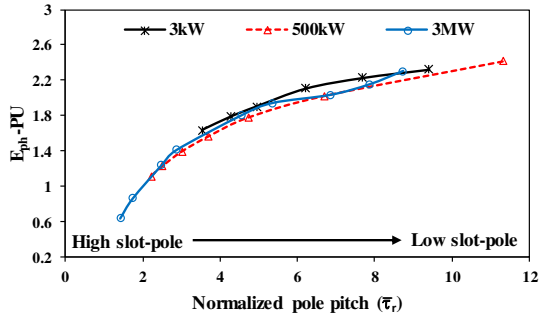

(a)

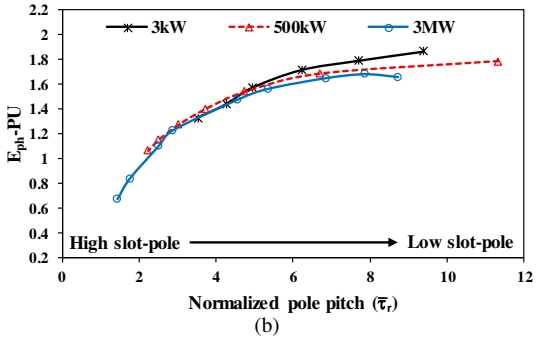

(b)

Fig. 19. Comparison of E_{ph-PU} between Vernier machines with power rating 3kW, 500kW, and 3MW calculated using (a) equation (27) and (b) FEA. For a given power rating, the result is presented across different slot/pole numbers (x-axis) which is represented here as normalized pole pitch ($\bar{\tau_r}$).

As the Vernier machine designs are globally optimized, there are minor variations in variables like δ_s and θ_o for different power ratings with the same normalized pole pitch. This can lead to the curves not being perfectly overlapped to each other. However, neglecting those variations between designs, the induced EMF performance of Vernier machine is largely unaffected by scaling of the machine.

It is worth noting that the airgap flux density (B_{P_r}) and airgap diameter (D_g) may not be the same between conventional SPM and SPM-V machines as assumed in the above ideal case. Considering those differences, the comparison as predicted by FEA for E_{ph-PU} is shown in Fig. 19(b). Although the same trend as predicted by (27) can be observed, there is significant drop in the magnitude of E_{ph-PU}. This is mainly due to the reduced airgap flux density (B_{P_r}) in the SPM-V machine compared to the conventional SPM machine for the same normalized pole pitch value. The flux density ratio, K_B [ratio of fundamental airgap flux density (B_{P_r}) of SPM-V machine to conventional SPM machine] is compared in Fig. 20.

It shows a 20-25% lower airgap flux density for the SPM-V machine compared with the conventional SPM machine. Nevertheless, very importantly, the Vernier machine still can achieve almost 60-80% higher EMF values than conventional machine even for multi-MW power ratings. This makes them very attractive for direct drive wind power

applications because the Vernier design can be used to reduce the machine size and also the magnet consumption.

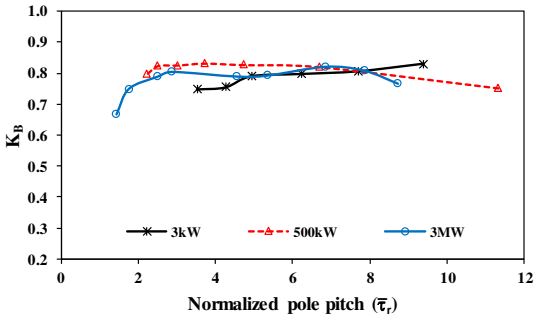

Fig. 20. Comparison of fundamental radial airgap flux density ratio (K_B) between conventional SPM and SPM-V machine for different power ratings.

B. On-Load Torque

The comparison of per unit torque ($Torque_{PU}$) predicted by FEA for different power ratings is shown in Fig. 21. For each power rating, as the armature current is maintained the same between the SPM and SPM-V machines, $Torque_{PU}$ should in theory follow the same trend as E_{ph-PU}. However, the influence of saturation at high normalized pole pitch (low slot/pole number combination) is clearly observed for the 500kW and 3MW machines which have much higher electrical loading than the 3kW machine as shown in TABLE I. The low slot/pole number designs are more prone to high saturation due to its large coil inductance and thereby high armature reaction [39]. Nevertheless, the SPM-V machine can still achieve excellent torque density of about 62% higher than that of the conventional SPM machine even at 3MW power level.

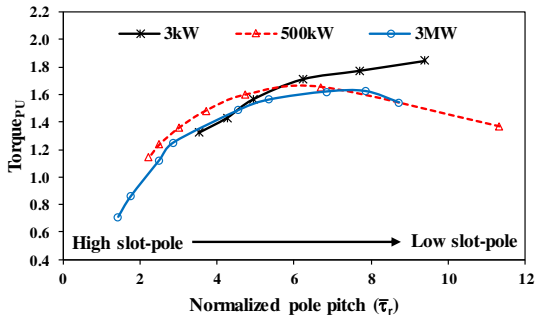

Fig. 21. Comparison of $Torque_{PU}$ between Vernier machines with power rating of 3kW, 500kW, and 3MW calculated using FEA. For a given power rating, the result is presented across different slot/pole numbers (x-axis) which is represented here as normalized pole pitch ($\bar{\tau}_r$).

C. Power Factor

For wind generator, a good power factor (>0.9) is also a very critical requirement. The comparison of the power factor between SPM and SPM-V machines for different power ratings are shown in Fig. 22. For each power rating, the power factor for SPM-V machine is calculated for different slot/pole number combinations and compared with the reference conventional SPM machine. Unlike the trends observed in EMF and torque, the power factor of the SPM-V machine is significantly dropped with increase in electrical loading (power rating) across all slot/pole number designs. However, the power factor of the conventional SPM machine remained almost unaffected with scaling.

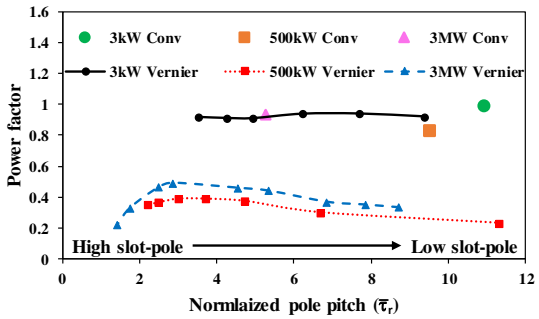

Fig. 22. Comparison of power factor between Vernier machines with power rating of 3kW, 500kW, and 3MW calculated using FEA. For a given power rating, the result is presented across different slot/pole numbers (x-axis) which is represented here as normalized pole pitch ($\bar{\tau}_r$).

A simple analytical expression of power factor has been derived to explain the phenomenon observed in Fig. 22. Neglecting the voltage drop due to armature resistance, the power factor of a conventional SPM machine can be given as [41]

$$PF = \frac{1}{\sqrt{1+\left(\frac{I_{ph}X_{ph}}{E_{ph-c}}\right)^2}} \tag{34}$$

where I_{ph} is the phase current, X_{ph} is the phase reactance and E_{ph-c} is the open-circuit phase EMF. The phase reactance of SPM-V machine (X_{ph-v}) is almost gear ratio (G_r) times higher than that of the conventional SPM machine (X_{ph}) and this is true for all the slot/pole number combinations of SPM-V machine [38]. Therefore, the power factor for SPM-V machine can be represented as

$$PF = \frac{1}{\sqrt{1+\left(\frac{I_{ph}X_{ph-v}}{E_{ph-v}}\right)^2}} = \frac{1}{\sqrt{1+\left(\frac{I_{ph}G_rX_{ph}}{E_{ph-v}}\right)^2}} \tag{35}$$

Substituting $I_{ph} = \frac{\pi D_g Q}{2mT_{ph}}$ in (37) gives

$$PF = \frac{1}{\sqrt{1+[K_t]^2}} \tag{36}$$

with

$$K_t = \left(\frac{\pi D_g X_{ph}}{2mT_{ph}}\right)\left(\frac{QG_r}{E_{ph-v}}\right) \tag{37}$$

where Q is the electrical loading of the SPM-V, m is the number of phases and T_{ph} is the number of turns (in series) per phase. The trend of power factor versus K_t is shown in Fig. 23.

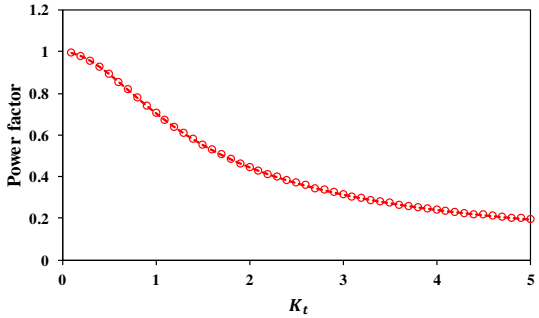

Fig. 23. Variation of power factor with variable K_t.

It is observed that with low values of K_t (<<1) the power factor can be really high (close to unity) and with K_t > 1, the power factor significantly drops below 0.6. From (39), it is observed that the value of K_t is largely dominated by the product of electrical loading and operating gear ratio. For the same power rating (same electrical loading), the SPM-V machine with much larger gear ratio (G_r=5) is expected to have much lower power factor than the conventional SPM machine (G_r=1). This difference between SPM-V and SPM machines increases with increasing electrical loading (power rating). The comparison of K_t between SPM and SPM-V machines for different power ratings calculated using FEA is shown in TABLE III.

TABLE III. COMPARISON OF TERM K_t FOR DIFFERENT POWER RATINGS BETWEEN CONVENTIONAL SPM AND SPM-V

Machine Type	Design number	K_t 3kW	500kW	3MW
Conventional	0	0.1	0.66	0.37
Vernier	1	0.42	4.17	2.82
Vernier	2	0.35	3.15	2.65
Vernier	3	0.36	2.46	2.5
Vernier	4	0.46	2.35	2.03
Vernier	5	0.45	2.35	1.92
Vernier	6	0.43	2.52	1.76
Vernier	7		2.67	1.9
Vernier	8			2.83
Vernier	9			4.3

It is observed that, for the SPM-V machines with low electrical loading, e.g. 3kW machine, K_t<<1 and therefore can attain very high power factor (>0.9) which is comparable to conventional SPM machine. However, with increasing electrical loading (almost 10 times that of 3kW), the value of K_t increases considerably (>>1) for the 500kW and 3MW SPM-V machines. This drastically reduces the power factor to < 0.5. It is therefore concluded that for low power ratings, the SPM-V machine shows very good overall performance compared to conventional SPM machine because of its high power factor (>0.9) and substantially high torque density. However, for large power direct drive machines with high electrical loading, the poor power factor would remain as a main challenge for this class of machines.

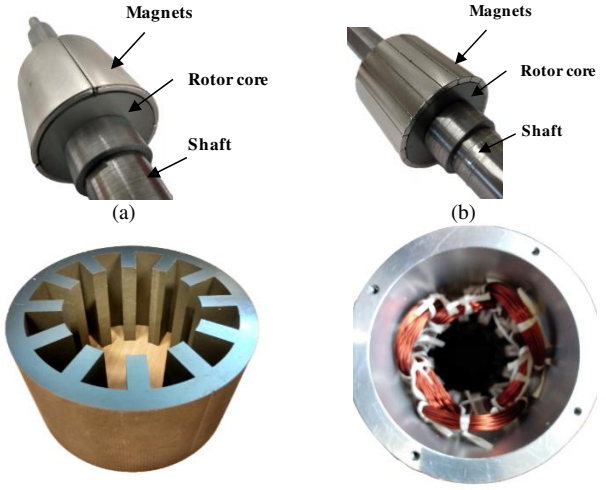

Fig. 24. Prototypes of conventional SPM and SPM-V machines showing (a) rotor of conventional SPM machine with 4 poles, (b) rotor of SPM-V machine with 20 poles, (c) stator core with 12 slots and (d) complete assembly of stator core with winding and housing.

VI. Experimental Validation

To validate the analytical model and 2D FEA results, a conventional SPM machine and a SPM-V machine prototypes are manufactured as shown in Fig. 24. The key parameters of the prototypes are given in TABLE IV. The conventional SPM and SPM-V rotors are shown in Fig. 24(a) and (b), respectively. The stator cores without winding and with integer slot winding (slot/pole/phase equals to 1) are shown in Fig. 24(c) and (d) respectively.

TABLE IV. KEY PARAMETERS OF PROTOTYPE

	Conventional SPM	SPM-V
Stator slot number	12	
Rotor pole pair number	2	10
Airgap length (mm)	1	
Stack length(mm)	50	
Stator outer diameter(mm)	100	
Magnet height, h_m(mm)	3	
Magnet B_r, μ_r	1.2, 1.01	
Rated speed (rpm)	400	

A. Induced EMF

The comparison of the measured and 2D FEA predicted phase EMF for conventional SPM and SPM-V machines is shown in Fig. 25. The induced EMF generated by SPM-V machine is observed to be more sinusoidal compared to the conventional SPM machine. The spectra of phase EMF are shown in Fig. 25(b), which clearly shows higher harmonic contents in the conventional SPM machine. This is mainly due to the slotting effect, i.e. 3 slots under each rotor pole, leading to significantly higher harmonics in the EMF.

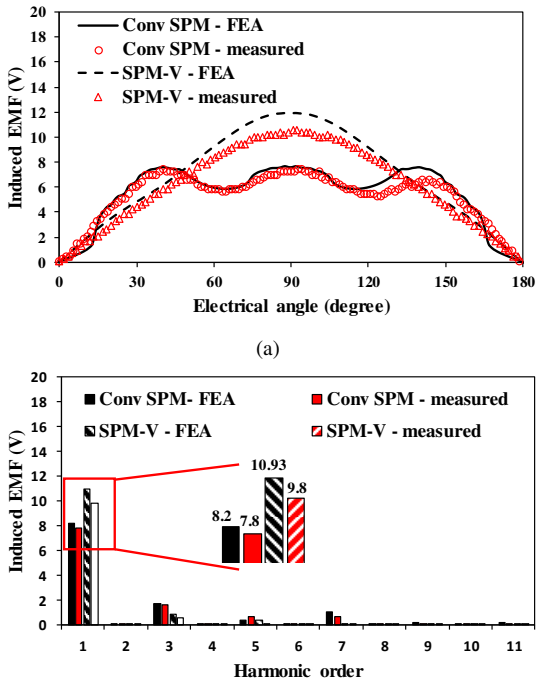

Fig. 25. Comparison of (a) waveforms and (b) harmonic spectra of predicted and measured phase EMF for conventional SPM and SPM-V machine prototypes.

TABLE V. COMPARISON OF ANALYTICALLY PREDICTED EMF WITH MEASURED AND 2D FEA RESULTS

Machine Type	Fundamental peak phase EMF (V) Measured	2D FEA	Analytical
SPM-V	9.8	10.93	11.3

It has been found that the measured peak value of the fundamental EMF is in good agreement with the simulation

for the conventional SPM machine (within 5% error). However, for the SPM-V machine, the measurement is showing a deviation of around 10% compared to the FEA and analytical simulations. The phase EMF predicted analytically for the SPM-V machine using (26) is shown in TABLE V and is found to be in good agreement with 2D FEA prediction.

The cause of the deviation for the measured EMF of the SPM-V machine is mainly due to the gap between adjacent magnets created by manufacturing tolerance and assembly error, as shown in Fig. 26. The magnet arc coefficient (α_p) used in the 2D FEA simulation is 1. The sensitivity of induced EMF with α_p is studied for both the machines. The value of α_p is varied from 0.98 to 1 and the induced EMF is compared for both the machines, as shown in Fig. 27. It is observed that unlike the conventional SPM, the SPM-V is very sensitive to the gap between the magnets. When α_p is 0.99, the predicted phase EMF of the SPM-V machine matches very well with the measured result. There is no difference between the phase EMF for $\alpha_p = 0.99$ and $\alpha_p = 0.98$. For the SPM-V machine, an α_p of 0.99 results in a gap length of 86μm, which is very reasonable considering the clearance required for gluing magnets on the rotor surface.

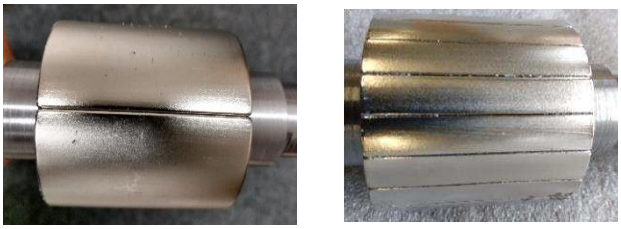

(a) (b)

Fig. 26. Gap between adjacent magnets due to manufacturing tolerances and assembly error in (a) conventional SPM machine and (b) SPM-V machine.

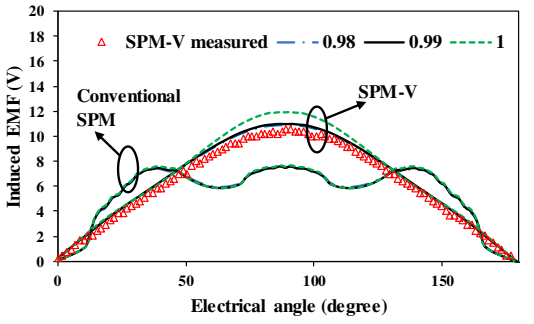

(a)

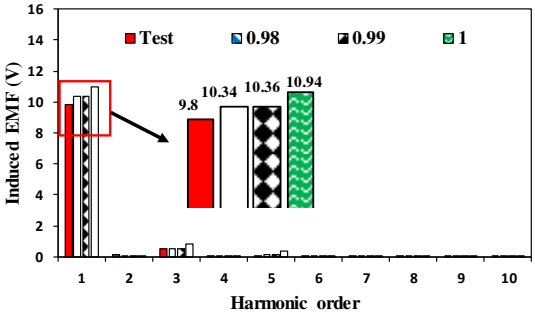

(b)

Fig. 27. Comparison of change in phase EMF (a) waveforms and (b) harmonic spectra (only for SPM-V machine) with variation in magnet arc coefficient (α_p) from 0.98 to 1 between conventional SPM and SPM-V machines. The measured phase EMF for the SPM-V is also included for comparison.

B. *Cogging Torque and On-Load Torque*

The methodology used for measuring the cogging torque and on-load torque is the same as detailed in [42]. The test setup for the measurement is shown in Fig. 28. The rotor is kept stationary, which is connected to a beam of 300mm in length having a suspended weight to measure the applied force on the digital scale. The torque can be simply calculated by using the measured force multiplied by the length of the beam (300mm). To measure the force (and torque) at different rotor positions, the stator is rotated, which leads to a relative angular motion between the stator and the rotor.

The comparison between the measured and 2D FEA predicted cogging torques for the conventional SPM and SPM-V machines is shown in Fig. 29. For the SPM-V machine, an α_p of 0.99 is used in the 2D FEA for comparison with the measurement. It is observed that the simulated results are in good agreement with the measured ones. The cogging torque for conventional SPM machine is found to be significantly higher than the Vernier machine. This is due to the fact that it has much lower Lowest Common Multiple (LCM) between the slot number and rotor pole number than the Vernier machine, i.e. LCM(12,4) = 12 for the conventional machine while LCM(12,20) = 60 for the Vernier machine. It is found in [43] that higher LCM generally leads to lower cogging torque.

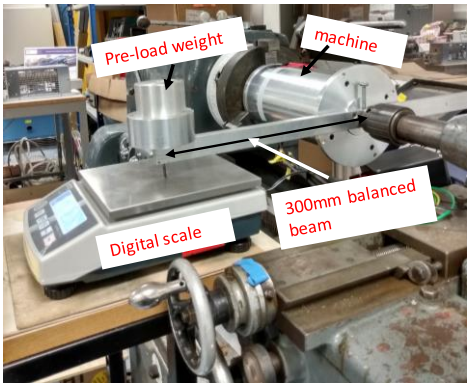

Fig. 28. Test setup for measuring on-load static torque and cogging torque.

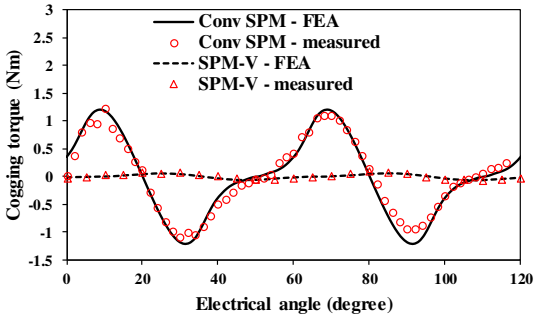

Fig. 29. Comparison between measured and 2D FEA predicted cogging torques for conventional SPM and SPM-V machines.

For measuring the on-load static torque, the same test setup as shown in Fig. 28 is used. However a DC current is injected into the phase A, which is connected in series with the other two parallel connected phases (B&C). This will allow 3-phase currents to satisfy the following relationship, $I_A = I$, $I_B = I_C = -I/2$, where I is the DC current, thus simulating one static point of 3-phase supply. Similar to

cogging torque measurement, the stator is rotated to measure the force using the digital scale. The comparison of the measured and 2D FEA predicted static torques at a peak phase current of 4 A is shown in Fig. 30. The static torque measurements are in good agreement with the simulations. There is significant contribution of cogging torque towards static torque of the conventional SPM machine as shown in Fig. 31. The measured torque shows that the fundamental peak torque for the SPM-V machine is almost 27% higher than the conventional SPM machine.

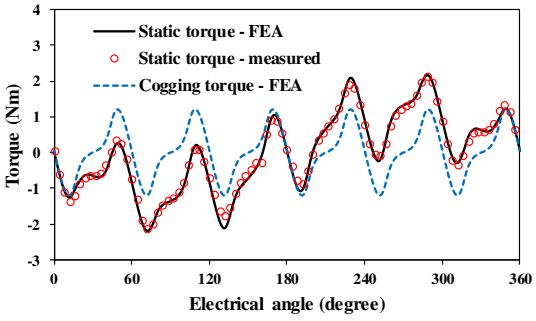

(a)

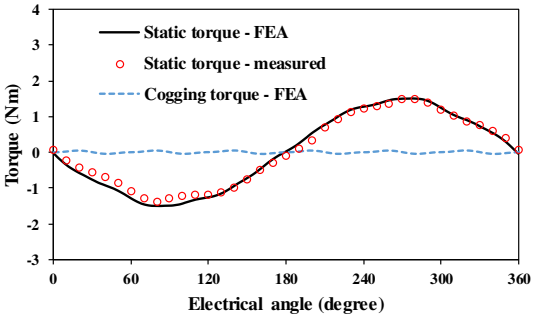

(b)

Fig. 30. Comparison between measured and 2D FEA predicted on-load static torques for (a) conventional SPM machine and (b) SPM-V machine.

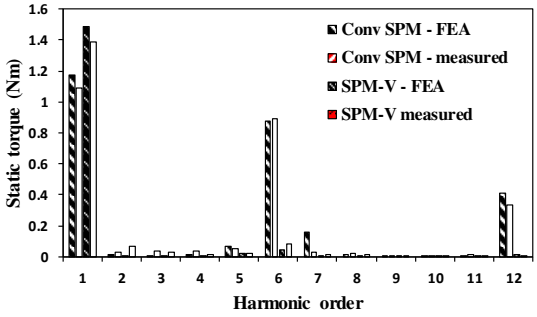

Fig. 31. Comparison of harmonic spectra between measured and 2D FEA predicted on-load static torques for conventional SPM machine and SPM-V machine at 4 A peak phase current.

The static torque measurement was repeated for different peak phase currents and the fundamental torque (from Fast Fourier Transform) is compared between the conventional SPM and SPM-V machines as shown in Fig. 32. The 2D FEA results are in line with the measurements. The fundamental torque is showing almost linear relationship with phase current for both machines, with SPM-V consistently showing higher torque capability.

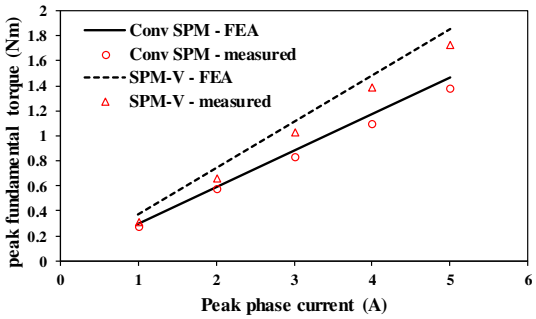

Fig. 32. Comparison between measured and 2D FEA predicted peak fundamental torques with varying peak phase current for the conventional SPM and SPM-V machines.

VII. Conclusion

The impact of scaling from 3kW to 3MW on performance of SPM Vernier machines is investigated. The study shows that with scaling, the induced EMF performance is unaffected for the same normalized pole pitch. However, due to magnetic saturation, this is not the case for average torque particularly at low slot/pole number and high electrical loading. It is also revealed that, unlike conventional SPM, the power factor of the SPM-V significantly drops with increased electrical loading due to scaling effect. The existing analytical equation for induced EMF of Vernier machine has been improved by introducing a simple leakage factor derived from geometrical parameters and also accounting for the impact of the $(Z+P_r)^{\text{th}}$ order working harmonics of radial airgap flux density for different slot/pole number designs. The study revealed that the leakage factor and $(Z+P_r)$ term become crucial for high and low slot/pole number designs respectively and cannot be neglected. The final analytical calculations considering both the $(Z+P_r)^{\text{th}}$ order working harmonics and the leakage factor have been validated by the FEA results. Both conventional SPM and SPM-V machine prototypes have been built, and the FEA results have been validated by measured ones.

Acknowledgment

This work is supported by the UK EPSRC Prosperity Partnership “A New Partnership in Offshore Wind” under Grant No. EP/R004900/1.

Appendix

For a Vernier machine, designed with slot/pole number satisfying the rule $Z - P_r = P_s$, the slot opening (b_o) can be expressed as

$$b_o = \delta_s \times \tau_s \tag{38}$$

where τ_s is the stator slot pitch. For integer-slot winding configuration (considered in this study)

$$b_o = \delta_s \times C_p \times \frac{2P_s}{N_s} \tag{39}$$

Number of stator slots (N_s) and coil pitch (C_p) can be represented in terms of gear ratio (G_r) as

$$N_s = (G_r + 1)P_s \tag{40}$$

$$C_p = G_r \tau_r \tag{41}$$

Substituting (40) and (41) in (39) yields

$$b_o = \frac{2G_r}{G_r + 1}\delta_s\tau_r \tag{42}$$

REFERENCES

[1] H. Polinder, J. A. Ferreira, B. B. Jensen, A. B. Abrahamsen, K. Atallah, and R. A. McMahon, 'Trends in wind turbine generator systems', *IEEE J. Emerging Sel. Top. Power Electron.*, vol. 1, no. 3, pp. 174–185, Sep. 2013.

[2] Z. Zhang, A. Chen, A. Matveev, R. Nilssen, and A. Nysveen, 'High-power generators for offshore wind turbines', *Energy Procedia*, vol. 35, pp. 52–61, Jan. 2013.

[3] D. Bang, H. Polinder, G. S. Shrestha, and J. A. Ferreira, "Review of generator systems for direct-drive wind turbines," in *European Wind Energy Conference & Exhibition*, *Belgium*, 2008, vol. 31, pp. 1–11.

[4] H. Polinder, F. F. A. van der Pijl, G.- de Vilder, and P. J. Tavner, 'Comparison of direct-drive and geared generator concepts for wind turbines', *IEEE Trans. Energy Convers.*, vol. 21, no. 3, pp. 725–733, Sep. 2006.

[5] R. S. Semken, M. Polikarpova, P. Roytta, J. Alexandrova, J. Pyrhonen, J. Nerg, A. Mikkola, J. Backman, "Direct-drive permanent magnet generators for high-power wind turbines: benefits and limiting factors," *IET Renew. Power Gener.*, vol. 6, no. 1, pp. 1–8, Jan. 2012.

[6] R. Qu, Y. Liu, and J. Wang, "Review of superconducting generator topologies for direct-drive wind Turbines," *IEEE Trans. Appl. Supercond.*, vol. 23, no. 3, pp. 5201108–5201108, 2013.

[7] Y. Terao, M. Sekino, and H. Ohsaki, "Comparison of conventional and superconducting generator concepts for offshore wind turbines," *IEEE Trans. Appl. Supercond.*, vol. 23, no. 3, pp. 5200904–5200904, June. 2013.

[8] J. Wang, R. Qu, Y. Liu, J. He, Z. Zhu, and H. Fang, "Comparison study of superconducting wind generators with HTS and LTS field windings," *IEEE Trans. Appl. Supercond*, vol. 25, no. 3, pp. 1–6, June. 2015.

[9] Y. Alexandrova, R. S. Semken, and J. Pyrhonen, 'Permanent magnet synchronous generator design solution for large direct-drive wind turbines: Thermal behavior of the LC DD-PMSG', *Appl. Therm. Eng.*, vol. 65, no. 1–2, pp. 554–563, Apr. 2014.

[10] K. Atallah and D. Howe, "A novel high-performance magnetic gear," *IEEE Trans. Magn.*, vol. 37, no. 4, pp. 2844–2846, Jul. 2001.

[11] K. Atallah, J. Rens, S. Mezani, and D. Howe, "A novel 'pseudo'' direct-drive brushless permanent magnet machine," *IEEE Trans. Magn.*, vol. 44, no. 11, pp. 4349–4352, Nov. 2008.

[12] L. Jian, K. T. Chau, and J. Z. Jiang, "A magnetic-geared outer-rotor permanent-magnet brushless machine for wind power generation," *IEEE Trans. Ind. Appl.*, vol. 45, no. 3, pp. 954–962, May 2009.

[13] A. Toba and T. A. Lipo, "Generic torque- maximizing design methodology of surface permanent- magnet Vernier machine," *IEEE Trans. Ind. Appl.*, vol. 36, no. 6, pp. 1539–1546, Nov. 2000.

[14] K. Okada, N. Niguchi, and K. Hirata, "Analysis of a Vernier motor with concentrated windings," *IEEE Trans. Magn.*, vol. 49, no. 5, pp. 2241–2244, May 2013.

[15] Y. Oner, Z. Q. Zhu, and W. Chu, "Comparative study of Vernier and interior PM machines for automotive application," *Proc. IEEE Vehicle Power and Propulsion Conf.*, Hangzhou, China, Oct. 2016, pp. 1-6.

[16] D. W. Li, R. H. Qu, and J. Li, "Topologies and analysis of flux-modulation machines," presented at the *Proc. Energy Convers. Congr. Expo. (ECCE)*, 2015, pp. 2153–2160.

[17] J. Li, K. T. Chau, J. Z. Jiang, C. Liu, and W. Li, "A new efficient permanent-magnet Vernier machine for wind power generation," *IEEE Trans. Magn.*, vol. 46, no. 6, pp. 1475–1478, Jun. 2010.

[18] X. L. Li, K. T. Chau, and M. Cheng, "Analysis, design and experimental verification of a field-modulated permanent-magnet machine for direct-drive wind turbines," *IET Electr. Power Appl.*, vol. 9, no. 2, pp. 150–159, Feb. 2015.

[19] Y. Gao, R. Qu, D. Li, J. Li, and G. Zhou, "Design of a dual-stator LTS Vernier machine for direct-drive wind power generation," *IEEE Trans. Appl. Supercond.*, vol. 26, no. 4, Jun. 2016.

[20] W. L. Li, T. W. Ching, and K. T. Chau, "A new high-temperature superconducting Vernier permanent-magnet machine for wind turbines," *IEEE Trans. Appl. Supercond.*, vol. 27, no. 4, Jun. 2017.

[21] C. Yicheng, P. Pillay, and A. Khan, 'PM wind generator topologies', *IEEE Trans. Ind. Appl.*, vol. 41, no. 6, pp. 1619–1626, Nov/Dec. 2005.

[22] J. Y. Chen, C. V. Nayar, and L. Y. Xu, 'Design and finite-element analysis of an outer-rotor permanent-magnet generator for directly coupled wind turbines', *IEEE Trans. Magn.*, vol. 36, no. 5, pp. 3802–3809, Sep. 2000.

[23] A. Grauers, "Design of direct-driven permanent magnet generators for wind turbines," Ph.D. dissertation, Chalmers Univ. Technol., Goteborg, Sweden, 1996.

[24] Z. Q. Zhang, A. Matveev, R. Nilssen, and A. Nysveen, "Ironless permanent-magnet generators for offshore wind turbines," *IEEE trans. Ind. Appl.*, vol. 50, no. 3, pp. 1835–1846, May 2014.

[25] L. Wu, R. Qu, D. Li, and Y. Gao, "Influence of pole ratio and winding pole numbers on performance and optimal design parameters of surface permanent-magnet Vernier machines," *IEEE Trans. Ind. Appl.*, vol. 51, no. 5, pp. 3707–3715, Sep. 2015.

[26] T. Zou, D. Li, R. Qu, D. Jiang, and J. Li, "Advanced high torque density PM Vernier machine with multiple working harmonics," *IEEE Trans. Ind. Appl.*, vol. 53, no. 6, pp. 5295–5304, Nov. 2017.

[27] L. Wu, R. Qu, and D. Li, "Analysis of eddy current losses in surface-mounted permanent magnet Vernier machines," *Proc. IEEE Int. Conf. Electr. Mach. Drives*, 2017, pp. 1–6.

[28] M. Raza, W. L. Zhao, T. A. Lipo, and B. I. Kwon, "Performance comparison of dual airgap and single airgap spoke-type permanent-magnet Vernier machines," *IEEE Trans. Magn.*, vol. 53, no. 6, pp. 1–4, Jun. 2017.

[29] D. W. Li, R. H. Qu, J. Li, L. Y. Xiao, L. L. Wu, and W. Xu, "Analysis of torque capability and quality in Vernier permanent-magnet machines," *IEEE Trans. Ind. Appl.*, vol. 52, no. 1, pp. 125–135, Jan. 2016.

[30] Z. S. Du and T. A. Lipo, "Torque performance comparison between a ferrite magnet Vernier motor and an industrial interior permanent magnet machine," *IEEE Trans. Ind. Appl.*, vol. 53, no. 3, pp. 2088–2097, May 2017.

[31] S. Hyoseok, N. Niguchi, and K. Hirata, "Characteristic analysis of surface permanent-magnet Vernier motor according to pole ratio and winding pole number," *IEEE Trans. Magn.*, vol. 53, no. 11, pp. 1–4, Nov. 2017.

[32] B. Kim and T. A. Lipo, "Operation and design principles of a PM Vernier motor," *IEEE Trans. Ind. Appl.*, vol. 50, no. 6, pp. 3656–3663, Nov./Dec. 2014.

[33] B. Heller and V. Hamata, *Harmonic field effects in induction machines*. Amsterdam, The Netherlands: Elsevier, 1977, pp. 54-67.

[34] Z. Q. Zhu and D. Howe, "Instantaneous magnetic field distribution in brushless permanent magnet DC motors. III. Effect of stator slotting," *IEEE Trans. Magn.*, vol. 29, no. 1, pp. 143–151, Jan. 1993.

[35] M. Choi and B. Kim, 'Calculation of PM Vernier motors using an improved air-gap permeance function', *IEEE Trans. Magn.*, vol. 55, no. 6, pp. 1–5, Jun. 2019.

[36] B. Gaussens, E. Hoang, O. de la Barriere, J. Saint-Michel, M. Lecrivain, and M. Gabsi, "Analytical approach for air-gap modeling of field-excited flux-switching machine: No-load operation," *IEEE Trans. Magn.*, vol. 48, no. 9, pp. 2505–2517, Sep. 2012.

[37] L. R. Huang, J. H. Feng, S. Y. Guo, J. X. Shi, W. Q. Chu, and Z. Q. Zhu, "Analysis of torque production in variable flux reluctance machines," *IEEE Trans. on Energy Convers.*, vol. 32, no. 4, pp. 1297–1308, Dec. 2017.

[38] H. Li, Y. Liu, and Z. Q. Zhu, "Comparative study of air-gap field modulation in flux reversal and Vernier permanent magnet machines," *IEEE Trans. Magn.*, vol. 54, no. 11, pp. 1–6, Nov. 2018.

[39] D. Kumar K.P, G. J. Li, Z. Q. Zhu, M. P. Foster, D. A. Stone, A. Griffo, M. Odavic, R. Clark, A. Thomas, "Influence of demagnetization on selecting the optimum slot/pole number combination for 3MW surface mounted permanent magnet vernier machine," *IEEE Int. Conf. Electr. Mach. Sys.*, Harbin, China, pp. 1–6, Aug. 2019.

[40] M. R. Dubois, H. Polinder, and J. A. Ferreira, 'Influence of air gap thickness in Transverse Flux Permanent Magnet (TFPM) generators for wind turbine application', in *Proc. IEEE Young Researchers Symposium in Elec. Pow. Eng.* 2002, Leuven, Belgium.

[41] T. W. Ching, K. T. Chau, and W. Li, 'Power factor improvement of a linear vernier permanent-magnet machine using auxiliary dc field excitation', *IEEE Trans. Magn.*, vol. 52, no. 7, pp. 1–4, Jul. 2016.

[42] Z. Q. Zhu, 'A simple method for measuring cogging torque in permanent magnet machines', in Proc. *IEEE Power Energy Soc. General Meet.*, pp. 1–4, Jul. 26-30, 2009.

[43] Z. Q. Zhu and D. Howe, 'Influence of design parameters on cogging torque in permanent magnet machines', *IEEE Trans. on Energy Convers.*, vol. 15, no. 4, pp. 407–412, Dec. 2000.